



## Source Reconstruction of the 1969 Western Sulawesi, Indonesia, Earthquake and Tsunami

IGNATIUS R. PRANANTYO,<sup>1,2</sup>  ATHANASIOS CIPTA,<sup>3</sup> HASBI A. SHIDDIQI,<sup>4</sup> TOSHITAKA BABA,<sup>5</sup> and KENTARO IMAI<sup>6</sup>

**Abstract**—The island of Sulawesi, Indonesia, is located in a complex and tectonically active region, and has experienced tsunamis in the past. One of the major earthquake and tsunami events was the 23 February 1969 event that struck the Majene region in western Sulawesi Island. Interpretation of the historical accounts revealed that the Mw 7.0 earthquake generated strong intensity up to VIII on the Modified Mercalli Intensity scale. The earthquake was followed by an unusually high tsunami of 4 m that rapidly decayed within 25 km from the highest observation site. Hypocentre and earthquake mechanism analyses confirmed that it was an inland earthquake with a thrust mechanism. Ground motion modelling is able to reproduce the earthquake intensity but earthquake scenarios are unable to reconstruct the tsunami observations. A plausible solution to explain the tsunami report is from a combined scenario of an earthquake and a submarine mass failure of 0.5 km<sup>3</sup>.

**Keywords:** Eastern Indonesia, Sulawesi, earthquake, tsunami, submarine mass failure, ground motion, numerical simulation.

### 1. Introduction

Sulawesi Island, eastern Indonesia, is situated in a complex and tectonically active region (Hall, 2011; Hamilton, 1979; Satyana et al., 2011; Silver et al., 1983) that has experienced at least seven tsunamis

since 1950 (Fig. 1). However, there are few studies in the literature to discuss these events, particularly their source mechanism. Knowing the source of a past event is beneficial for understanding the source characteristic in a particular region. This study aims to investigate the 23 February 1969 earthquake and tsunami that struck the Majene region, western Sulawesi.

The earthquake hypocentre was inland, with a moment magnitude (Mw) of 7.0 (US Geological Survey<sup>1</sup>) or a surface-wave magnitude of 7.1 (ISC-EHB<sup>2</sup>), and had a thrust mechanism (Fitch, 1972). The earthquake triggered strong ground shaking that caused people to lose their balance, and rockfalls occurred at several locations (Soetardjo et al., 1985; Soloviev et al., 1992) (Fig. 2). The earthquake generated an unusually high tsunami which rapidly decayed within 25 km from where the highest tsunami height was observed (International Tsunami Information Center, 1969a, b) (Fig. 2). A combination of the earthquake and tsunami claimed more than 64 fatalities and damaged more than one thousand buildings in Majene. Tsunami catalogues reported that the tsunami was mainly caused by the earthquake (Latief et al., 2000; Prasetya et al., 2001), but no further detail was provided about the source mechanism.

The main objective of this study is to show the first insight into the plausible source mechanism of the tsunami. First, we briefly describe the regional tectonics of western Sulawesi and historical accounts of the event. We then reanalyse the earthquake parameters and perform ground motion and tsunami

---

**Supplementary Information** The online version contains supplementary material available at <https://doi.org/10.1007/s00024-022-03064-2>.

---

<sup>1</sup> Department of Civil Engineering, Brunel University London, London, UK. E-mail: [ignatiusryanpranantyo@gmail.com](mailto:ignatiusryanpranantyo@gmail.com)

<sup>2</sup> Present Address: REASK UK Ltd., 49 Greek Street, London W1D 4EG, UK.

<sup>3</sup> Geological Agency, Bandung, Indonesia.

<sup>4</sup> Department of Earth Science, University of Bergen, Bergen, Norway.

<sup>5</sup> Graduate School of Technology, Industrial and Social Sciences, Tokushima University, Tokushima, Japan.

<sup>6</sup> Research Institute for Marine Geodynamics Research and Development, Center for Earthquake and Tsunami Forecasting, Japan Agency for Marine-Earth Science and Technology, Yokosuka, Japan.

---

<sup>1</sup> <https://earthquake.usgs.gov/earthquakes/eventpage/iscgem812497/executive>.

<sup>2</sup> <http://isc.ac.uk> event id = 812497.

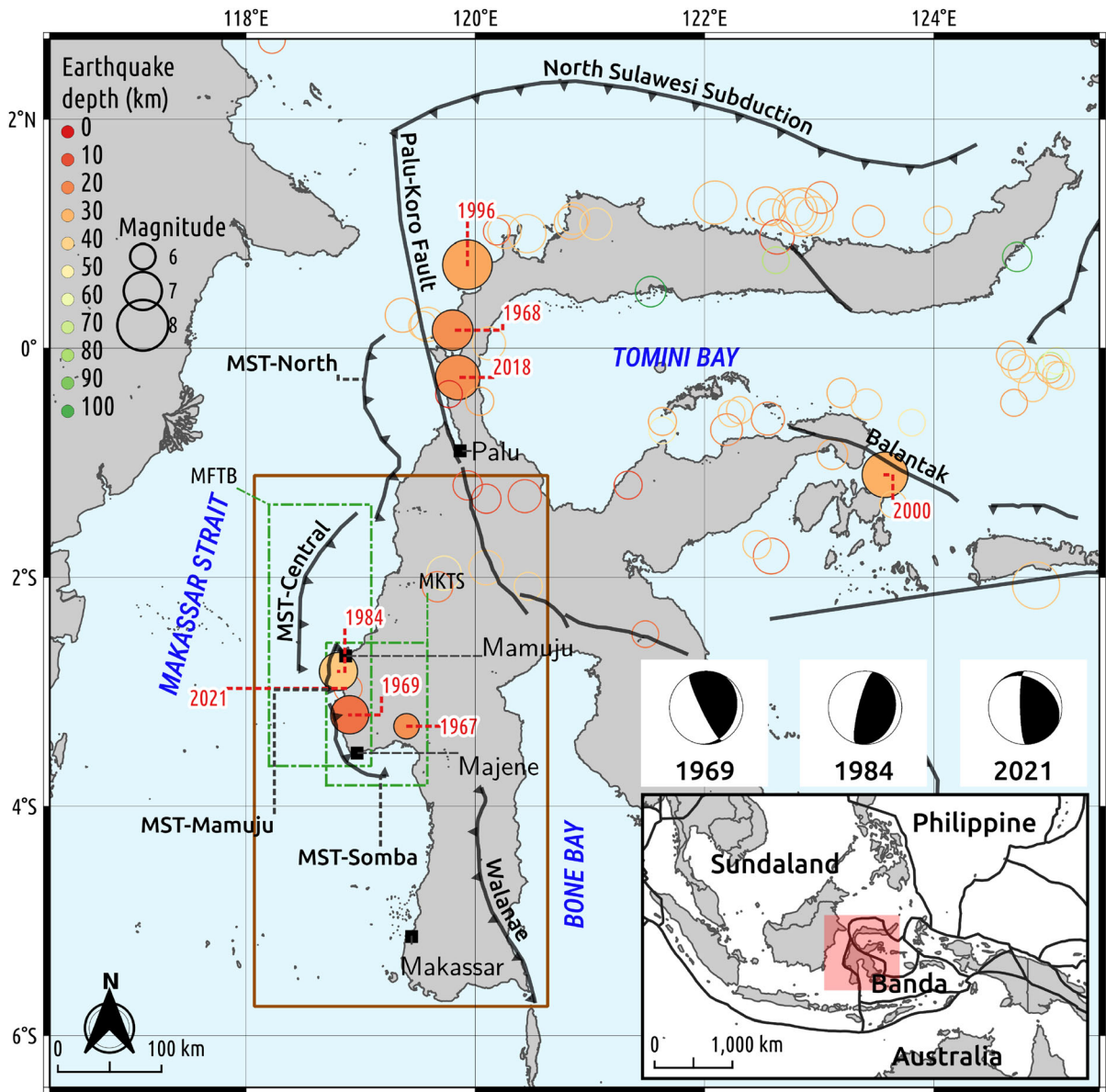


Figure 1

Map of regional tectonic setting of Sulawesi. Circles represent seismicity Mw 6.0 and above from 1950 to March 2021, taken from the United States Geological Survey (USGS) catalogue. Coloured circles represent hypocentral depth (0–100 km), and filled circles indicate an earthquake followed by a tsunami event. The radius of the circles indicates earthquake magnitudes as shown by the scale. Numbers denote years of major events which are discussed in the text. The inset map shows a simplified regional plate boundary (Bird, 2003). Beach balls represent focal mechanisms of the 1969 (this study), 1984 (USGS), and 2021 (USGS) earthquakes. MST, Makassar Strait Thrust; MFTB, Majene Fold Thrust Belt; MKTS, Majene/Kalosi Thrust System. Brown box indicates southern arm of Sulawesi Island

modelling to verify the historical accounts. Finally, we present and discuss the results.

## 2. Regional Tectonics of Western Sulawesi

The abundance of Neogene volcanic deposits, Late Eocene carbonate and Early Miocene sliiclastic

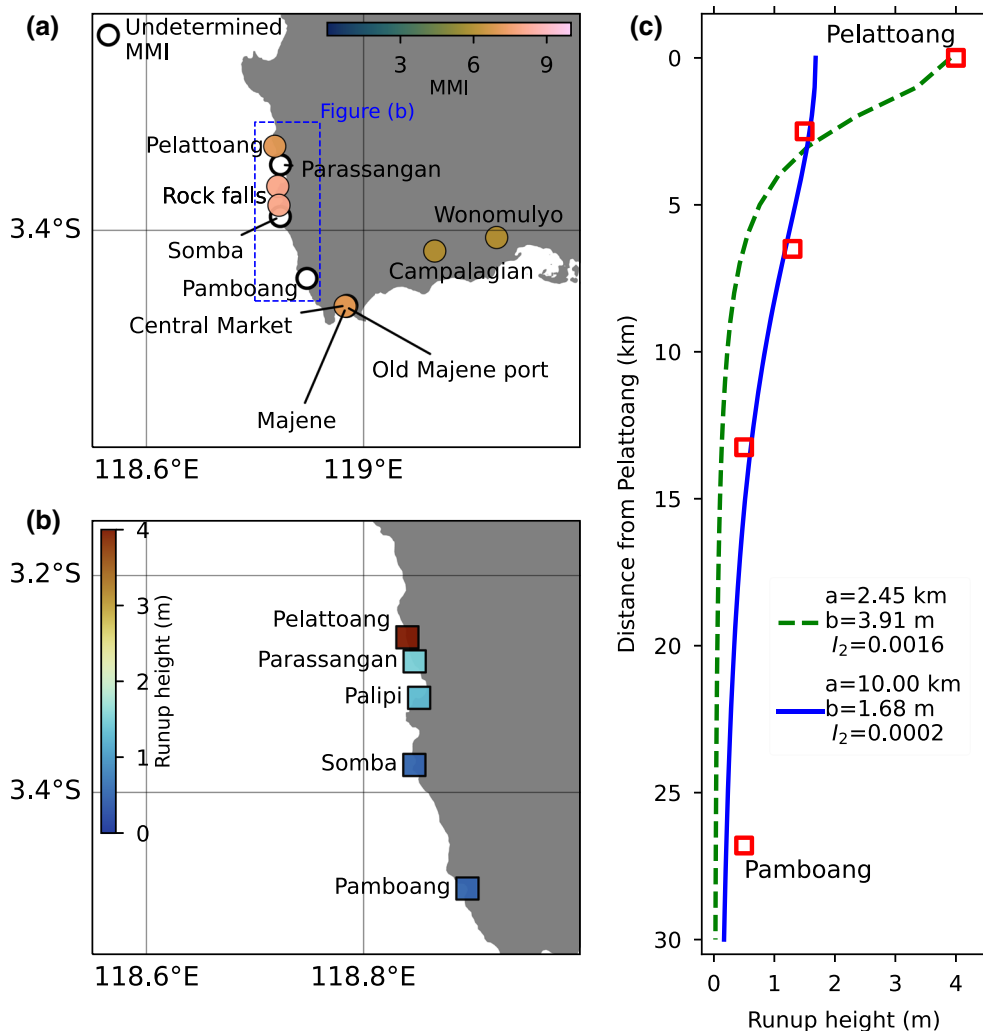


Figure 2

Historical accounts of the 1969 western Sulawesi, Indonesia, earthquake and tsunami. **a** Interpreted earthquake felt intensity on the Modified Mercalli Intensity (MMI) scale. The dashed blue box indicates the location of tsunami runup height observation, shown in **(b)**. **c** The  $I_2$  coefficient analysis following Okal and Synolakis (2004)

in the southern arm of Sulawesi (brown box in Fig. 1) is the main difference between this arm and the northern arm. Furthermore, from a geomorphological point of view, central-western Sulawesi has the most rugged terrain. On average, mountain ridges in this part of the island rise as high as 2000–3000 m, with maximum altitude of 3495 m (brown box in Fig. 1). All of these features reflect the complexity of the formation and tectonic history of the island. The island of Sulawesi consists of a number of fragments of lithosphere that display a complex geological

history of subduction, collision and local extension (Hall, 2011; van Leeuwen and Pieters, 2012).

The southern arm is underlain by a relatively strong, thick and cool lithosphere that was rifted from Australia and collided with Sundaland during the Cretaceous (Hall, 2011; Satyana et al., 2011). Since the Paleocene until early Eocene, most parts of Southeast Asia, southern Borneo and western Sulawesi have been emergent. Meanwhile, the volcanic arc that extended from the northern arm to the eastern part of western Sulawesi also emerged in the Eocene

Table 1

Summary of historical accounts of the 23 February 1969 western Sulawesi, Indonesia, earthquake and tsunami

Location <sup>1</sup>	Description <sup>2</sup>	MMI <sup>3</sup>	Tsunami height <sup>4</sup> (m)
Pelattoang, Tammero'do sub-village ( <i>dusun</i> in Indonesian)	People had difficulty standing	VII	4
Parassangan, Tallu Banua sub-village			1.5
Palipi Port			1.3
Somba			0.5
Pamboangan			0.5
Road between Somba and Parassangan	Rockfalls, landslide over Mandar formation	VIII	
Wonomulyo	Suffered damage	VI	
Campalagian	Suffered damage	VI	
Central market, Majene	Centre of the bazaar was heavily damaged	VII	
Old Majene Port, Majene	Land subsidence	VII	

<sup>1</sup> See locations at Fig. 2

<sup>2</sup> Earthquake felt intensity is compiled from Soetardjo et al. (1985) and Soloviev et al. (1992)

<sup>3</sup> Interpreted earthquake intensity according to the Modified Mercalli Intensity (MMI) scale

<sup>4</sup> Tsunami observations are from the International Tsunami Information Center (1969a, 1969b)

to late Oligocene. Shallow water carbonate was deposited during the Oligocene and continued until the Miocene in the southern and western-central Sulawesi (Satyana et al., 2011).

The tectonic structure in western Sulawesi, where it is part of the southern arm, is mainly affected by the Majene fold and thrust belt (MFTB in Fig. 1 and the Majene-Kalosi thrust system (MKTS in Fig. 1). This system is located in Makassar Strait offshore western Sulawesi, is north-south trending, moderately east-dipping, and accommodates an N80°E-trend with a convergence rate of 8.5 mm/year (Bellier et al., 2006). This thrust system is also known as the Sulawesi thrust zone separating Sundaland from Banda Block (Fig. 1) (Bergman et al., 1996; Rangin et al., 1999). Furthermore, the National Center for Earthquake Studies of Indonesia (Pusat Studi Gempa Nasional, 2018) divided this thrust system into four segments, i.e. North, Central, Mamuju, and Somba,

which are moving at a rate of 4–10 mm/year (MST in Fig. 1).

Western Sulawesi, in particular, experienced four major earthquakes between 1967 and 2021; three of them were followed by tsunamis (Fig. 1). All of the earthquake hypocentres were inland, located relatively close to each other, and had similar thrust mechanisms; presumably, they originated from the MST, but the details are still unknown. Following the 2018 Palu Bay tsunami and recent identification of submarine mass failures (SMFs) in Makassar Strait (Brackenridge et al., 2020; Nugraha et al., 2020), the possibility of a tsunami triggered by SMF cannot be ignored.

### 3. Data and Methodologies

#### 3.1. Interpretation of the Historical Accounts

We collected the earthquake and tsunami observations from the International Tsunami Information Center (1969a, b), Soetardjo et al. (1985), and Soloviev et al. (1992). We traced locations reported on a Google Earth map and updated the names to the current location name. Further, we interpreted the earthquake intensity report from qualitative description to quantitative data-type on the Modified Mercalli Intensity (MMI) scale. Our interpretation is

Table 2

Weighting scheme used in hypocentre determination

Travel-time residuals (s)	Weight (%)
0–3	100
3–6	75
6–9	50
9–12	25
> 12	0

described in Sect. 4 and summarised in Table 1 and Fig. 2.

### 3.2. Earthquake Parameter Analysis

We reanalysed the earthquake hypocentres of the mainshock and its aftershocks using the HYPOCENTER program integrated into the SEISAN package (Havskov and Ottemoller, 1999; Havskov et al., 2020) and the iasp91 velocity model (Kennet, 1991) to confirm that the hypocentre of the mainshock was inland. We utilised the first arriving P- and S-phases, depth phase (pP), and mantle phases (PP, SS, and PcP) from regional and teleseismic distance stations (Fig. S1a), as well as arrival time data from the ISC-EHB catalogue (<http://www.isc.ac.uk/ise-ehb/>) (Engdahl et al., 2020; Weston et al., 2018). The arrival time readings were obtained from the analogue seismograms, including the World-Wide Standardized Seismograph Network seismograms (Peterson and Hutt, 2014). We carefully examined the travel-time residuals and used only S-P arrival times instead of individual P- and S-arrivals for stations with timing issues, following Hurukawa and Maung (2011), to

minimise erroneous timing on the analogue seismogram readings. To further overcome the limitation of picking accuracy from the analogue seismograms, we applied a weighting scheme based on the travel-time residuals shown in Table 2. Furthermore, to evaluate the hypocentre uncertainty of the mainshock, we performed a 3-D grid search location, with a spatial resolution of 5 km × 5 km (horizontal), and ran the travel-time calculation for a depth range of 5 km to 25 km. To determine the final earthquake hypocentral depth, we performed a depth grid search by varying the earthquake depths (0–50 km, with 1 km and 2.5 km intervals) and fixed its epicentre using the RMSDEP program from the SEISAN package (Havskov and Ottemoller, 1999). The best solution is chosen based on the smallest root-mean-square-error (RMSE) value (Eq. 1), where  $obs_i$ ,  $pre_i$ , and  $N$  are observed, predicted, and number of observed points, respectively.

$$RMSE = \sqrt{\frac{\sum (obs_i - pre_i)^2}{N}} \quad (1)$$

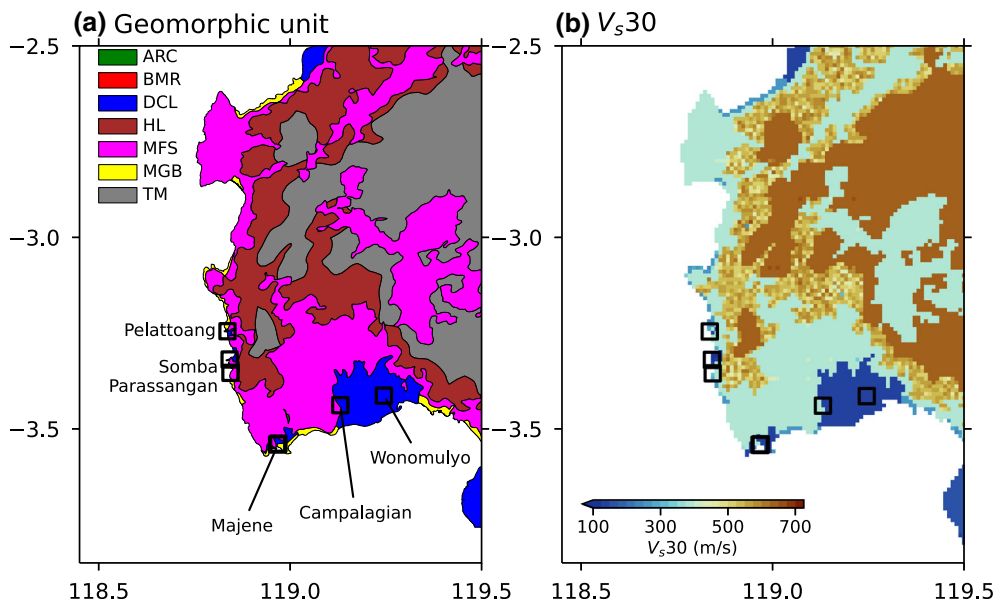


Figure 3

Map of **a** geomorphologic units and **b** the average shear wave velocity in the topmost 30 m of soil ( $V_{s30}$ ), created by following Matsuoka et al. (2006). ARC abandoned river channel, BMR back marsh, DCL delta and coastal lowland, HL hill, MFS mountain foot slope, MGB marine sand and gravel bars, TM: tertiary mountain

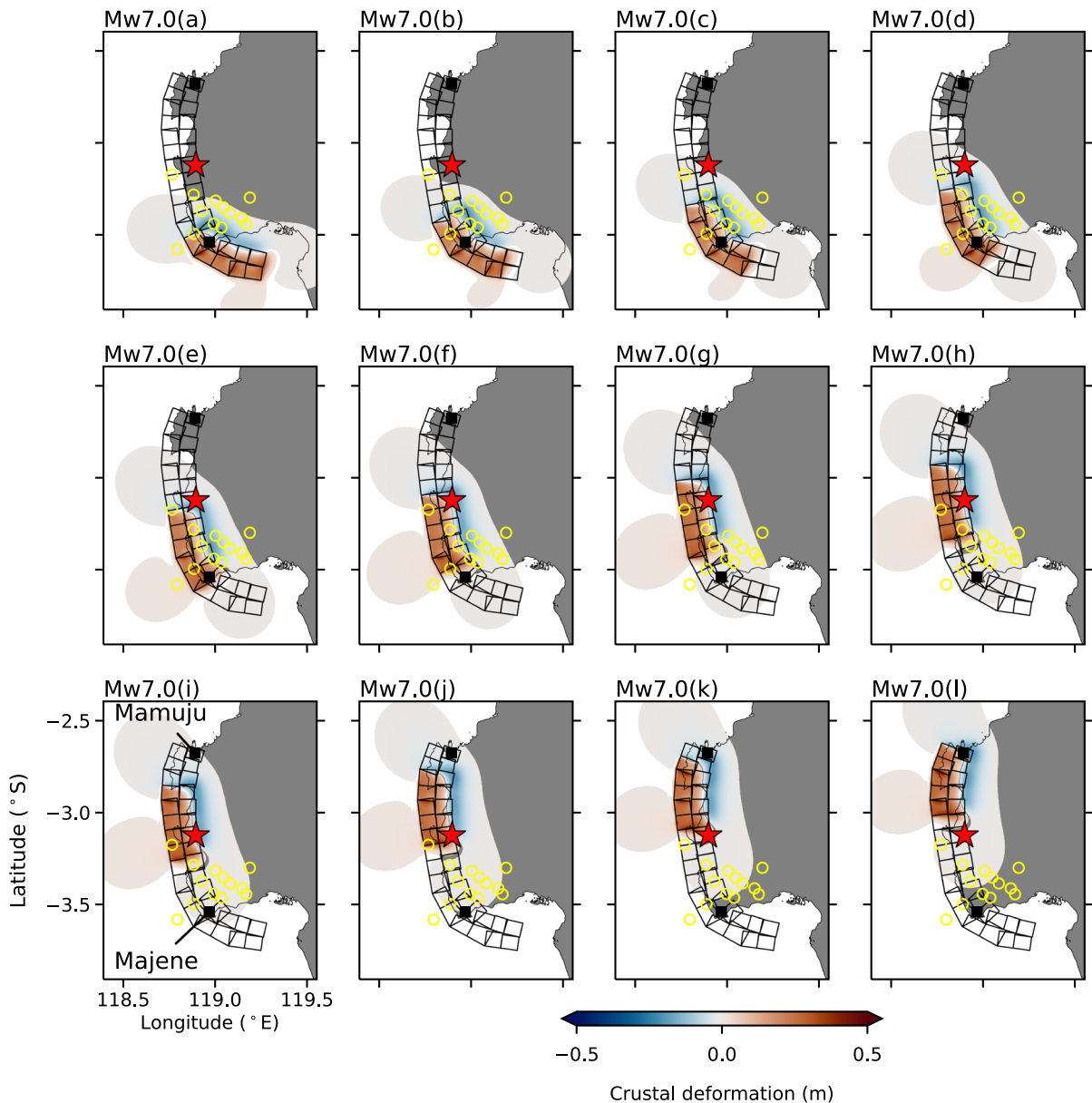


Figure 4

Mw 7.0 earthquake scenarios considered in this study for ground motion and tsunami modelling. Black hollow rectangular polygons show composite subfaults to define the earthquake rupture area. Red star and yellow circles are the earthquake mainshock and aftershock epicentres, respectively. Blue to red colourmap indicates crustal earthquake deformation. Black squares show locations of Majene and Mamuju

Fitch (1972) showed that the earthquake had a thrust mechanism (Table 2). To confirm the solution, we reanalysed the focal mechanism by utilising the first-motion polarities reported in the ISC-EHB catalogue. We used two software programs, FPFIT (Reasenber and Openheimer, 1985) and HASH (Hardebeck,

2002), which were integrated into the SEISAN package. Following Lentas (2017), we only used polarities of the direct P-waves at teleseismic distances (up to  $90^\circ$ ) from the epicentre (Fig. S1b).



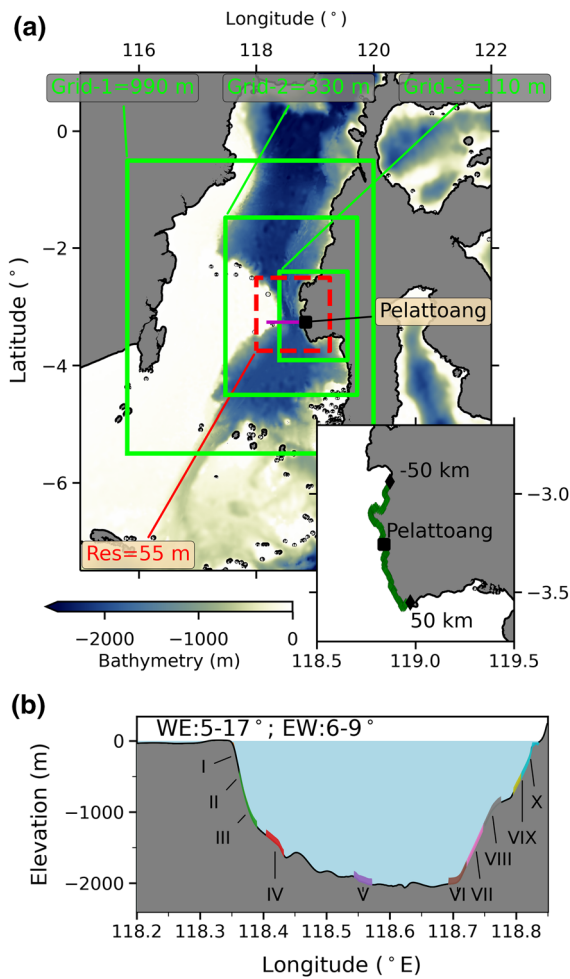


Figure 5

**a** Digital elevation model (DEM) used for tsunami modelling. Green boxes show nested domain model used for modeling tsunamigenic earthquake scenarios. SMF tsunami modelling is done on a single grid domain model shown in the red box. The inset figure shows locations where tsunami coastal tsunami height is collected from the model; the numbers 50 km and -50 km show the distance from Pelattoang. The magenta line represents the bathymetric profile shown in panel **b** of this figure. **b** Ten locations considered for the SMF locations shown by Roman numbers I, II, ..., X. Coloured polygons illustrate SMF 1.0 km<sup>3</sup> at different locations. Here, “WE” and “EW” are the range of slope angle along west to east and east to west bathymetric profiles. “Res” is an acronym for spatial model resolution of the grid

### 3.3. Tsunami Source Discriminant

We analysed the  $I_2$  coefficient (Eq. 2), a ratio between maximum tsunami height ( $b$ ) and lateral horizontal distance of tsunami height along the coastline ( $a$ ), where  $y$  is the distance along the shoreline and  $c$  is fixed at 0, as introduced by Okal

and Synolakis (2004). The  $a$  and  $b$  coefficients were estimated using non-linear least-squares fitting from the curve\_fit library in the Scipy package (Virtanen et al., 2020). The  $I_2$  coefficient analysis has been widely used to determine the dominant nature of a tsunami source (e.g. Fritz et al., 2007; Gerardi et al., 2008). According to Okal and Synolakis (2004), the tsunami observation could be caused by an earthquake if  $I_2$  is smaller than  $10^{-4}$ , or a landslide if it is larger than  $10^{-4}$ .

$$I_2 = \frac{b}{a}$$

$$\zeta(y) = \frac{b}{((y - c)/a)^2 + 1} \tag{2}$$

$$c = 0$$

### 3.4. Ground Motion Modelling

We performed ground motion modelling to validate felt intensity data using the OpenQuake Engine (Pagni et al., 2014). We estimated peak ground acceleration (PGA) according to the ground motion prediction (GMPE) of Boore et al. (2014), and the average shear wave velocity in the topmost 30 m of soil ( $V_s30$ ) to parameterise soil condition. The  $V_s30$  is estimated from the surface geology and topographic features (Fig. 3a), following the geomorphic approach introduced by Matsuoka et al. (2006). We used the  $V_s30$  dataset from Cipta et al. (2017) that has been used to study probabilistic seismic hazard in Sulawesi and successfully explained the pattern of destruction during the 2018 Palu earthquake (Cipta et al., 2020). Further, the estimated PGA is converted into MMI following Wald et al. (1999).

An Mw 7.0 earthquake would rupture over an area of 40–50 km (length) and 20 km (width) based

Table 3

Submarine mass failure (SMF) scenarios			
Volume (km <sup>3</sup> )	Length (km)	Width (km)	Thickness (m)
0.5	1.5	3.0	100
0.6	2.0	3.0	100
1.0	3.3	3.3	100

on estimates using the reverse fault scaling law of Thingbaijam et al. (2017). To accommodate the curvature shape of the MST, we built a composite fault plane consisting of 32 subfaults, and assumed that the Somba and Mamuju segments are on a fault plane system. The fault plane has a top and maximum bottom depth of 0.1 km and 20 km (Pusat Studi Gempa Nasional, 2018), respectively, with a dip angle of  $16^\circ$ . To determine the best rupture model that would fit the earthquake intensity dataset, we simply shifted the rupture area from the southern tip of Majene to the northern part of Mamuju, resulting in 12 rupture models (models Mw7.0(a) to Mw7.0(l) in Fig. 4, Table S1). The best-fit rupture model area is chosen based on the RMSE value (Eq. 1). This value is calculated as the difference between the observed and model intensity; the larger the value, the larger the difference.

### 3.5. Tsunami Modelling

Given the unusual height of the tsunami and the  $I_2$  coefficient (see Sect. 5.3), it is likely that another source mechanism was involved in this event. We tested three different source mechanisms: (1) earthquake, (2) submarine mass failure (SMF), and (3) a combination of earthquake and SMF. To validate the coastal tsunami height observations, we conducted tsunami modelling using the JAGURS code (Baba

Tsunami source	Computation layer	Resolution (m)	Box colour <sup>a</sup>
Earthquake	3 layers	990 : 330 : 110	Solid-green
Submarine mass failure (SMF)	1 layer	55	Dashed-red
Earthquake + SMF			

<sup>a</sup>See Fig. 5a

et al., 2015, 2019). We solved the non-linear shallow water wave equations in 2D spherical coordinates. A digital elevation model (Fig. 5a) for the tsunami modelling is built from a combination of the national bathymetric data (BATNAS: <https://tanahair.indonesia.go.id/portal-web>), bathymetric contours for a shallow coastal region (Lembar Pantai Indonesia: <https://portal.ina-sdi.or.id/downloadaoi>), and the Shuttle Radar Topography Mission 90 m (Jarvis et al., 2008, <https://srtm.csi.cgiar.org/>).

For the earthquake scenario, crustal earthquake deformation is estimated from the Okada (1985) dislocation formula, which is then used as the initial sea surface status after applying the Kajiura (1963) filter for modelling tsunami propagation. We tested 12 rupture models which were also used for the ground motion modelling and assumed a

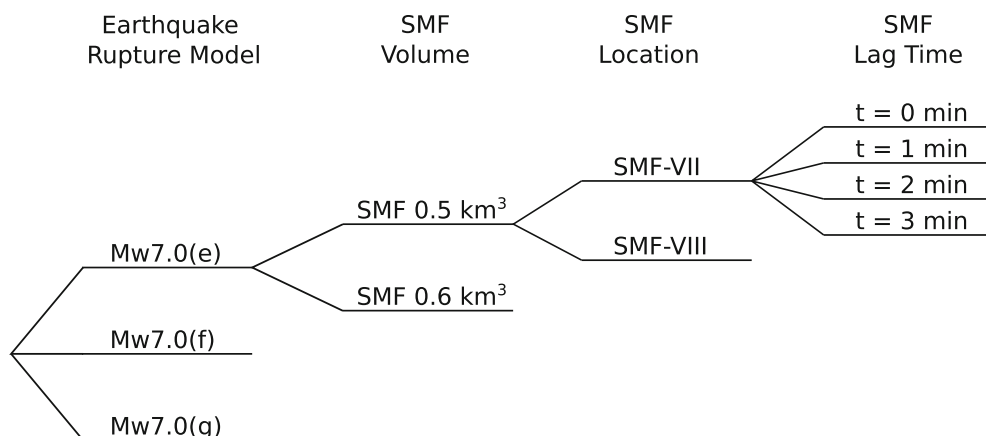


Figure 6

Schematic combination earthquake and submarine mass failure (SMF) scenarios. Earthquake rupture models are selected based on the top three best-fit models discussed in Sect. 5.2 and shown in Fig. S3. SMF volume and SMF location models are based on the result discussed in Sect. 5.4 and shown in Fig. S4, whereas SMF lag time is based on a trial-and-error approach. It leads to 48 combination scenarios = 3 earthquake rupture models  $\times$  2 SMF volumes  $\times$  2 SMF locations  $\times$  4 SMF lag time



homogeneous slip displacement model (models Mw7.0(a) to Mw7.0(l) in Fig. 4, Table S1).

For tsunamis generated by SMF sources, we used the two-layer model in JAGURS (Baba et al., 2019) following Imamura and Imteaz (1995). The tsunami propagation is modelled by coupling two layers of two flows that have different densities ( $\rho$ ), corresponding to seawater ( $\rho = 1000 \text{ kg m}^{-3}$ ) and turbidity (SMF,  $\rho = 1600 \text{ kg m}^{-3}$ ) currents. As modelling of SMF tsunamis involves large uncertainties over source parameters (e.g., shape, volume, location), we simplified SMF to a box shape and tested three volumes (Table 3) over ten different locations (Fig. 5b, shown in Roman numbers I, II, ..., X). We acknowledge that our box shape model might be too simple. However, a high-resolution elevation model is required to reproduce a more realistic source model for the SMF tsunami. In this study, there are no such available data for the analyses. Here, we assume an instantaneous SMF displacement model and we let the SMF fall freely controlled by the gravity and the bathymetry. The SMF starts to fall with velocity of  $0 \text{ m s}^{-1}$  and reaches a velocity up to  $\sim 55 \text{ m s}^{-1}$ , depending on its volume and location. In addition, we did not consider varying SMF density as it would increase the complexity in analysing the result and computation time. Moreover, varying the SMF densities is unlikely to change the final conclusion much, other than the SMF volume required.

For the combination earthquake-SMF source, we combined three best-fit earthquake ruptures, the model resulting smallest RMSE value and/or that giving closest modelled intensity to observed, two SMF volumes and locations models, and applied a lag time for the start time of the SMF (four lag time scenarios of 0 min, 1 min, 2 min, and 3 min), resulting in 48 scenarios (Fig. 6). Lag time means a time when the SMF model is added into tsunami model after the earthquake rupture.

We defined two domains for tsunami modelling, one for the earthquake source, and one for SMF and combination sources (Table 4). The domain of the tsunami model for the earthquake source consists of a three-level nested grid where the finest and coarsest model resolutions are  $0.001^\circ$  ( $\sim 110 \text{ m}$ ) and  $0.009^\circ$  ( $\sim 990 \text{ m}$ ), respectively (Fig. 5a). Because the two-layer model is expensive in terms the computation

time, we only conducted in a single grid level with resolution of  $0.0005^\circ$  ( $55 \text{ m}$ ) (Fig. 5a). We did not conduct inundation modelling because no high-resolution DEM is available. Instead of estimating the runup value by taking the offshore value and applying a coastal amplification function (e.g. Green's Law in Synolakis, 1991), we therefore extracted maximum simulated tsunami height at isobath 1 m (inset Fig. 5a), which we called coastal tsunami height, which is representative of tsunami runup height (e.g. Satake et al., 2006; Tinti et al., 2006). To select the best-fit scenario, we calculated the  $K$  and  $\kappa$  coefficients following Aida (1978) (Eq. 3).  $K$  represents the ratio between the maximum simulated tsunami ( $H_{sim}$ ) and tsunami height observation ( $H_{obs}$ ).  $\kappa$  is the standard deviation. We considered the model to be good when it gives  $K$  close to 1.0 with the smallest  $\kappa$ .

$$\begin{aligned} \log K &= \frac{1}{N} \sum_{i=1}^N \log K_i \\ \kappa &= \sqrt{\frac{1}{N} \sum_{i=1}^N ((\log K_i)^2 - (\log K)^2)} \\ K_i &= \frac{H_{obs_i}}{H_{sim_i}} \end{aligned} \quad (3)$$

#### 4. Historical Accounts

Western Sulawesi was shaken by an Mw 7.0 earthquake at 8:56 am (local time) on 23 February 1969. The earth-shaking caused rockfalls and landslides at several places along the road between Somba and Parassangan (Fig. 2). Large blocks of Neogene calcareous clay and tuff from the west flank of the hills were thrown off; we interpreted this experience as an MMI VIII. In Parassangan sub-village (*dusun* in Indonesian), no report on the damage was available; however, a 1.5 m tsunami height was reported.

To the south, about 5 km from Parassangan, a 1.3 m tsunami was reported at Palipi Port (Fig. 2). This port was located on the bay just off the road between Somba and Parassangan. Because the port

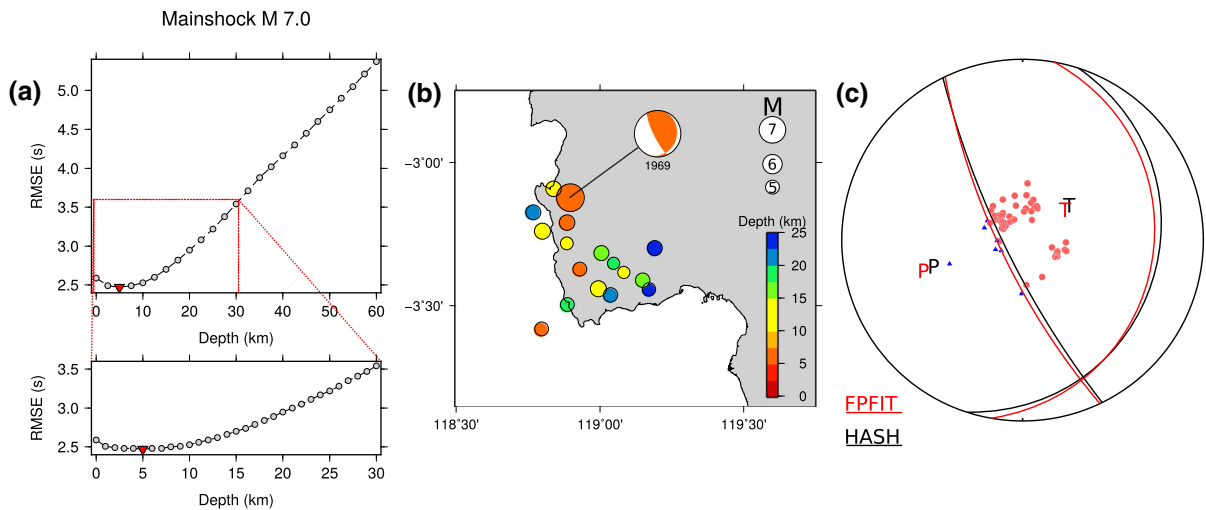


Figure 7

Earthquake location and focal mechanism analyses. **a** Root-mean-square-error (RMSE) residuals plots vs. mainshock depth. The red inverted triangle is the preferred depth. **b** Epicentres of the 1969 western Sulawesi earthquake sequence. The focal mechanism shows the mainshock location. **c** Focal mechanism solutions derived using FPFIT (red lines) and HASH (black lines). The polarities are also plotted in the lower hemisphere projection. The red circles are compression, and the blue triangles are dilatation

was relatively close to the rockfall site, an MMI of VII to VIII might have been experienced here.

Further to the north, about 4.8 km from Parasangan (Fig. 2), a living witness experienced “a big jolt” in Tammero’do Village, precisely at Pelattoang, where he was working in his garden. The *ninor* (meaning “earthquake” in local language) shaking was strong enough to cause a person to fall to the ground; we interpreted this as the minimum intensity of VII. According to the same eyewitness, very soon, a roaring sound was heard from the Makassar Strait followed by large oceanic waves. The *lembong tallu* (tsunami in local language) hit this place with a maximum height of 4 m.

The old Majene Port and Majene’s central market (Fig. 2) were standing onshore the bay facing south

to the Makassar Strait. During the earthquake, about 80% of the non-reinforced brick buildings in the town were severely damaged while three of them were completely destroyed; here most of the wooden houses were unaffected. According to Dowrick et al. (2008), decayed timber piles of houses experience damage when the earthquake intensity reaches MMI VIII or above; therefore, we inferred that a maximum MMI VII was possibly experienced in the city. Soetardjo et al. (1985) and Soloviev et al. (1992) reported that the outer side of the harbour may have subsided as well due to the earthquake.

Less information is available from Wonomulyo and Campalagian (Fig. 2). It was reported that these two densely populated districts suffered from the earthquake shaking. These two districts sit on

Table 5

Focal mechanism solutions of the 23 February 1969 western Sulawesi, Indonesia earthquake

Program used for analysis	Strike/Dip/Rake		Errors in Strike/Dip/Rake
	Nodal Plane 1	Nodal Plane 2	
FPFIT	10°/18°/124°	155°/75°/80°	10°/2°/16°
HASH	18°/16°/133°	154°/78°/79°	36°/8°/–
Fitch (1972)*	343°/18°/90°	163°/72°/90°	–

\*Converted from P- and T-axis solutions using FOCMEC package (Snook, 2003)

alluvium deposits (geomorphic unit of DCL in Fig. 3a). Soetardjo et al. (1985) and Soloviev et al. (1992) focused on the lithology of these areas, which they did not do in other locations. Therefore, the term “suffered” used by the aforementioned authors might be interpreted as a “rather strong shaking”. In an area composed of thick sediment as in a basin, seismic shaking in certain periods will be quite large in comparison with shaking in bedrock, although both areas are situated at the same distance and direction from the earthquake epicentre. The phenomena called seismic amplification was experienced in Wonomulyo and Campalagian. Thus, we assumed an intensity of VI was experienced by these two cities.

No precise information on the estimated tsunami arrival (ETA) time. According to Fikrie and Hardiansya (2018), a surviving eyewitness at Pelattoang said that the seawater suddenly receded. As soon as he witnessed seawater retreating from the shore, he ran around the village to warn villagers to evacuate to the nearby hills; fortunately, all villagers were saved.

## 5. Results and Discussion

### 5.1. Hypocentre and Focal Mechanism

The mainshock hypocentre of the 1969 western Sulawesi event was inland at a shallow depth (Fig. 7). However, an earthquake hypocentre determined using only distant stations can have large uncertainty. We obtained hypocentre errors of 9.5 km (latitude), 10.1 km (longitude), and 4.7 km (depth). The 3D grid search also confirmed that the earthquake depth is less than 10 km (Fig. 7a, Fig. S2), and the area with the lowest RMSE residual is inland (Fig. S2). Through three different approaches, we confirmed that our solution is stable and the mainshock is located inland. We also re-analysed the hypocentre of 15 other events that occurred between January 1969 and February 1970. We obtained that those 15 earthquake hypocentres were located in the southeast direction of the mainshock, with depth of less than 25 km (Fig. 7b). This information could give further information on the likelihood of the earthquake rupture area.

For the focal mechanism, the FPFIT and HASH programs give similar solutions and are consistent with the result from Fitch (1972), which is a thrust mechanism (Fig. 7c, Table 5). Given it was a shallow earthquake and was located at a greater distance from the main subduction tectonic fault (Fig. 1), we considered that the earthquake was triggered by a shallow crustal fault. To our knowledge, the closest fault is from the MST of the Somba or Mamuju segments (Pusat Studi Gempa Nasional, 2018), Nodal Plane 1 (Table 5), that dips eastward (Figs. 1, 7c)

### 5.2. Earthquake Rupture Model

The ground motion modelling is affected by the soil site condition. Western Sulawesi region can be divided into seven geomorphic units (Fig. 3a), i.e. tertiary mountains (TM), mountain foot slope (MFS), hill (HL), abandoned river channel (ARC), delta and coastal lowland (DCL), and marine sand and gravel bar (MGB). As it is dominated by wavy to steep topography, the TM and MFS are prevalent. The DCL is popping up in the southern part of the province in an area composed of Quaternary sediments where Campalagian, Wonomulyo, and Majene sit. Other locations significantly affected by the 1969 earthquake are located along the coastal area composed mainly of MGB (Fig. 3a).

Areas located in a flat morphology and composed of Quaternary sediments have significantly low  $V_{s,30}$  compared to the rest (Fig. 3b). In western Sulawesi, those low  $V_{s,30}$  areas can be classified into two units, i.e. MGB in a slim area along the coastal plain and DCL in a large groundwater basin in the province which is composed of Quaternary sediments. The value of  $V_{s,30}$  in this area is in the range 140–260 m/s and the soil softness in these units might be responsible for the large damage during the 1969 earthquake. In contrast, the rock of high mountains of the TM unit has  $V_{s,30}$  higher than 650 m/s. MFS and HL lie between the high mountain and coastal plain, which have  $V_{s,30}$  in the range of 400–600 m/s.

From ground motion modelling of 12 rupture model scenarios shown in Fig. 4, three scenarios of Mw7.0(f), Mw7.0(g) and Mw7.0(h) resulted in similar models with respective RMSE of 0.51, 0.43, and

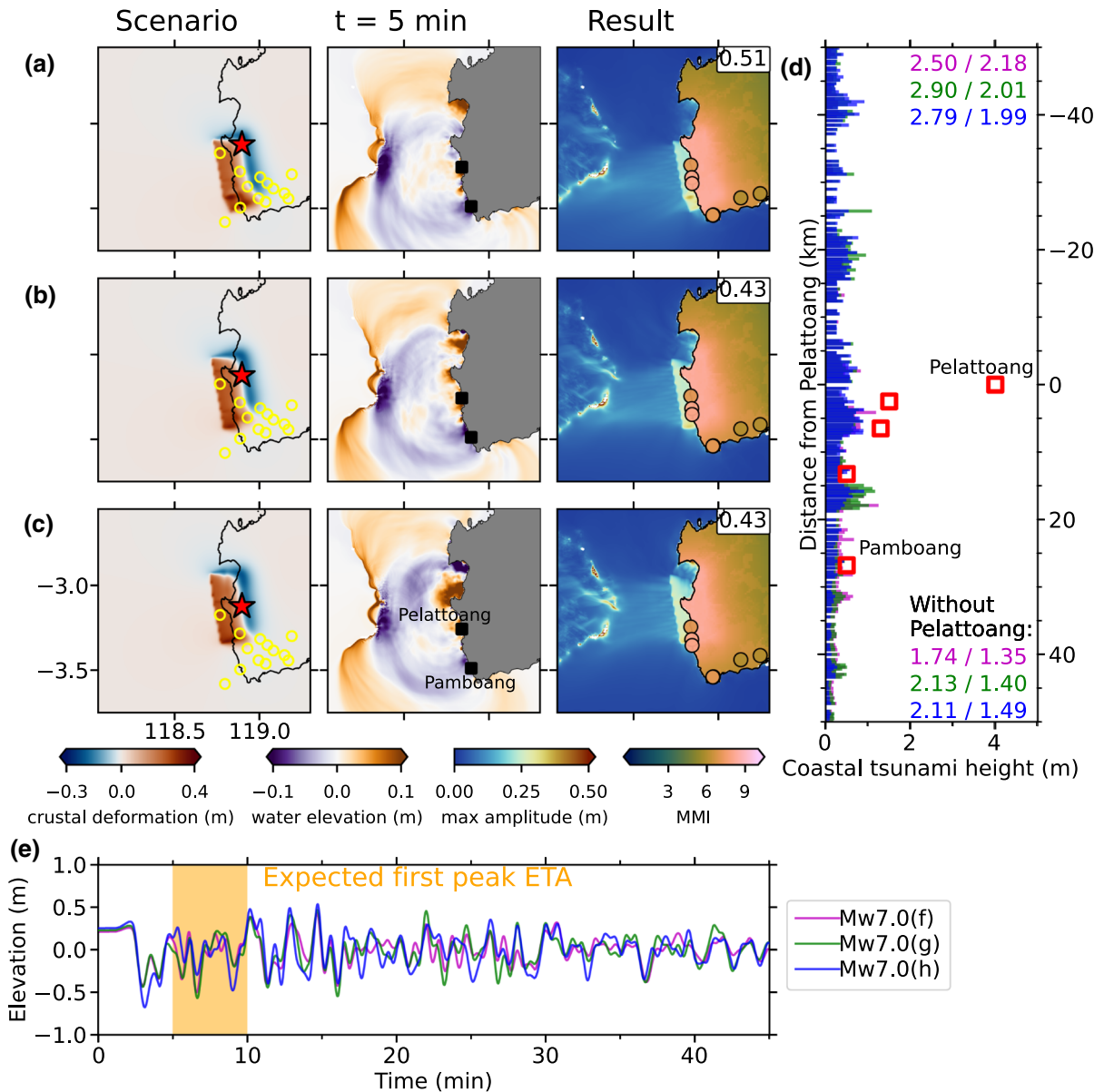


Figure 8

Selected tsunamigenic earthquake modelling results from rupture model **a** Mw7.0(f), **b** Mw7.0 (g), and **c** Mw7.0 (h). Sub-figures in panels **a–c** show the crustal deformation model (left panel), tsunami elevation at  $t = 5$  min (middle), and ground motion and tsunami modelling results. Red star and yellow circles represent earthquake epicentre and their aftershocks. Number shows RMSE from the ground motion modelling. **d** Maximum coastal tsunami heights with numbers show  $K / \kappa$  coefficients. **e** Tsunami waveform at Pelattoang

0.43, respectively (Fig. 8). These numbers are significantly smaller than the other scenarios, which have RMSE in the range from 0.64 to 1.24 (Fig. S3a). Scenario Mw7.0(f) effectively predicted the ground motion in Majene City and two rock fall spots on the road between Parassangan and Somba, resulting in an

MMI of VII. However, in Pelattoang, Wonomulyo and Campalagian, where MMIs of VII, VI and VI were estimated, respectively, the models over-predicted. Scenarios Mw7.0(g) and Mw7.0(h) greatly predicted intensity at six out of eight sites of macroseismic investigation. In Campalagian and

Pelattoang, the models overestimated by one intensity point. By overlaying the rupture model against the earthquake aftershocks, rupture model Mw7.0(f) covers most of the aftershocks compared to scenarios Mw7.0(g) and Mw7.0(h) (Fig. 8). Since the RMSE from scenario Mw7.0(f) is just slightly higher than model Mw7.0(g) and Mw7.0(h), we picked Mw7.0(f) as the best-fit rupture model to explain the earthquake intensity data (Fig. 8).

Insufficient historical information regarding the shaking impact leads to inaccuracy of intensity determination. A bias comes from the flawed site parameter and simplification of rupture model added in a bias into ground motion models. Consequently, finding a perfect fault model becomes a challenging job. Furthermore, our ground motion modelling relies on a selection of GMPE. However, no GMPE for Sulawesi and Indonesia is currently available (Rudyanto, 2014). Here, we used the GMPE from Boore et al. (2014) which is developed based on the global shallow crustal earthquake database.

### 5.3. The Unusual Tsunami Height

The unusual tsunami height of 4 m at Pelattoang and its rapid decay to 0.5 m within 25 km distance was potentially caused by a non-seismic source, in this case a landslide. We obtained  $I_2 = 1.6 \times 10^{-3}$  from historical accounts of coastal tsunami heights, indicating that the nature of the tsunami source was most likely a landslide (dashed green curve in Fig. 2c). This is 16-times the threshold for tsunamis caused by an earthquake based on the criterion developed by Okal and Synolakis (2004). By removing the 4-m tsunami height at Pelattoang, the outcome becomes  $I_2 = 2 \times 10^{-4}$ , which is still twice as large as the threshold (blue curve in Fig. 2c). It is noted that the  $I_2$  analysis is only based on five tsunami observations from an uneven distribution dataset.

The above analysis is confirmed by tsunami modelling of earthquake scenarios. The majority of the earthquake crustal deformation from our Mw 7.0 scenarios are located inland (scenarios Mw7.0(f), Mw7.0(g) and Mw7.0(h) in Fig. 8). Consequently, the maximum simulated tsunami height along the Majene coastline is relatively small; it is  $\sim 0.5$  m for all scenarios (Fig. S3b). All scenarios can reproduce

the 0.5-m tsunami height at Majene and Somba, but fail at the other three places, particularly at Pelattoang. If we exclude the data at Pelattoang, rupture models Mw7.0(d) to Mw7.0(h) give the lowest  $K$  and  $\kappa$  values, but these models still underestimate the observation by  $K = 1.74$  and  $\kappa = 1.36$  (Mw7.0(e) in Fig. 8d).

Anomalously high tsunami height, such as at Pelattoang, might be associated with amplification due to local topography effects (e.g. bay, harbour). Therefore, we conduct a visual observation from available imagery satellite data (Fig. S6), and confirm that Pelattoang is located along a “plain” coastal area. Similar evidence was observed for the 1992 Flores Island (Tsuji et al., 1995) and the 2006 Southern Java tsunamis (Fritz et al., 2007). An extreme tsunami runup height of 26 m (1992 Flores Island) and 21 m (2006 Southern Java) was measured, where the local average of the flow depth was 3–5 m and 7–8 m, respectively. The authors suggested that a possible local submarine mass movement was involved in these events. Therefore, this possibility can be considered in this event.

Furthermore, a 4-m tsunami height can also be achieved by adjusting the earthquake rupture model parameters: (i) fix the rupture area and its magnitude, then reduce the fault parameter rigidity to increase the fault slip model or (ii) fix the magnitude, maintain its rigidity and use a smaller rupture area to gain larger slip model. These two possibilities could reproduce a 4-m tsunami height at Pelattoang but will (i) overestimate or (ii) underestimate the tsunami observation at other places, respectively. Moreover, these scenarios will not fit the earthquake intensity data.

As the earthquake epicentre is near the coastline, most of the earthquake rupture is inland. Consequently, the tsunami generated by the earthquake alone is limited. The rupture model could be moved further westward (to the sea) so that the whole rupture model is in the sea. However, the earthquake rupture model will not fit with the tectonic setting in the region. Moreover, as the rupture is far from the land, this possible scenario will produce smaller earthquake intensity against data. Based on the numerical modelling results and above analyses, a landslide source was likely involved in this event.



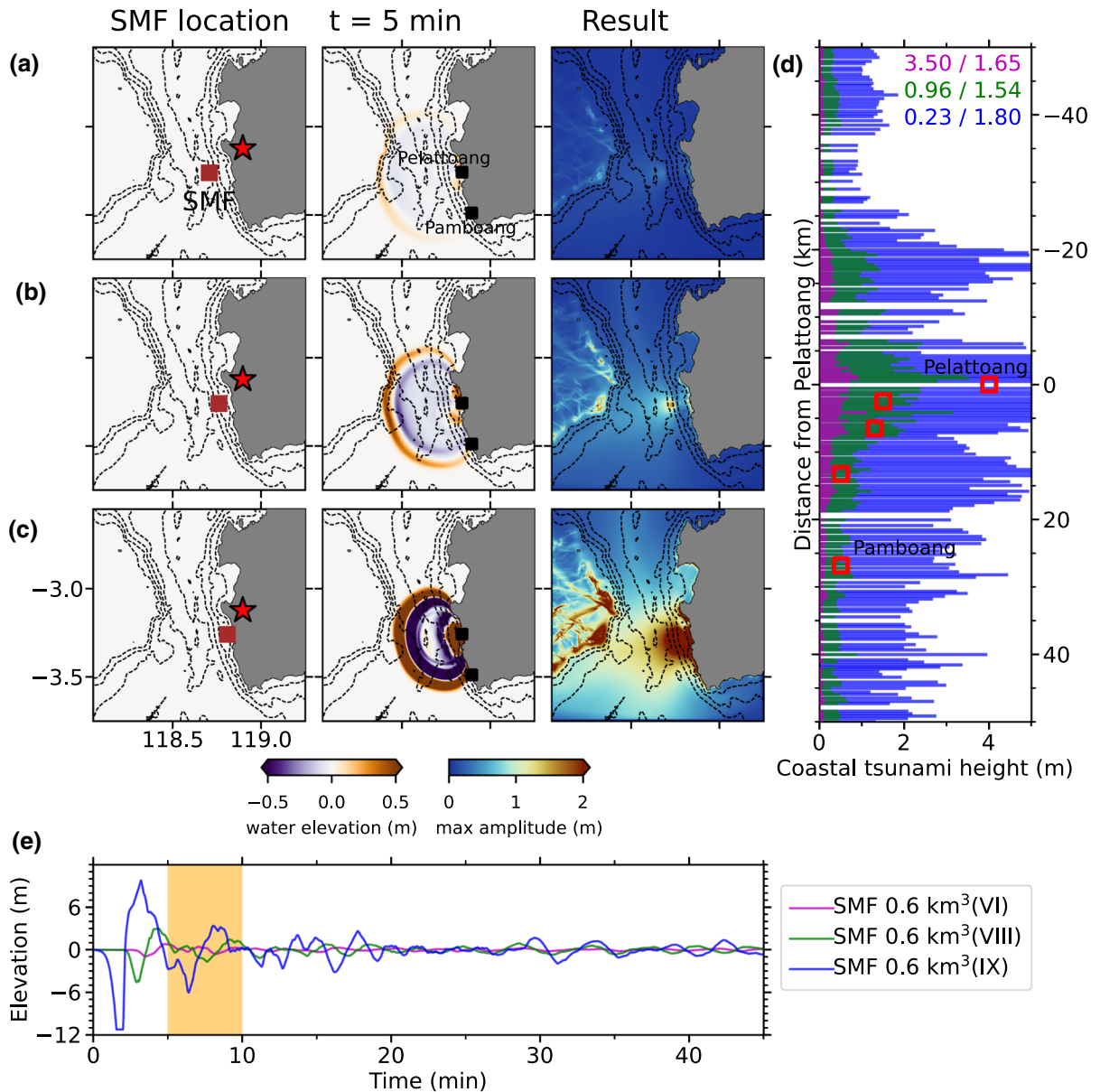


Figure 9

Selected submarine mass failure (SMF) tsunami scenarios from **a** SMF 0.6 km<sup>3</sup>(IV), **b** SMF 0.6 km<sup>3</sup>(VIII), and **c** SMF 0.6 km<sup>3</sup>(IX). Left to right panels show the SMF location (brown square), tsunami elevation at  $t = 5$  min, and tsunami max amplitude, respectively. Dashed contours are water depth at 500 m, 1000 m, 1500 m, and 2000 m. **d** Maximum coastal tsunami heights with numbers show  $K/k$  coefficients. **e** Tsunami waveform at Pelattoang

#### 5.4. Earthquake-Triggered Landslide Tsunami

Pelattoang, where the unusual tsunami height was observed, is situated between two deep basins of the Makassar Strait. It has deep bathymetry ( $\sim 2100$  m) with a steep slope angle of up to  $17^\circ$  and a narrow channel (50–60 km wide) (Fig. 5). A report by ten

Brink et al. (2009) showed that a landslide tsunami might occur and start at a bathymetry with a slope less than  $6^\circ$ . Furthermore, Brackenridge et al. (2020) hypothesised that the Indonesian Trough Flow that passes the Makassar Strait potentially creates slope instability. Along the Makassar Strait itself, SMFs



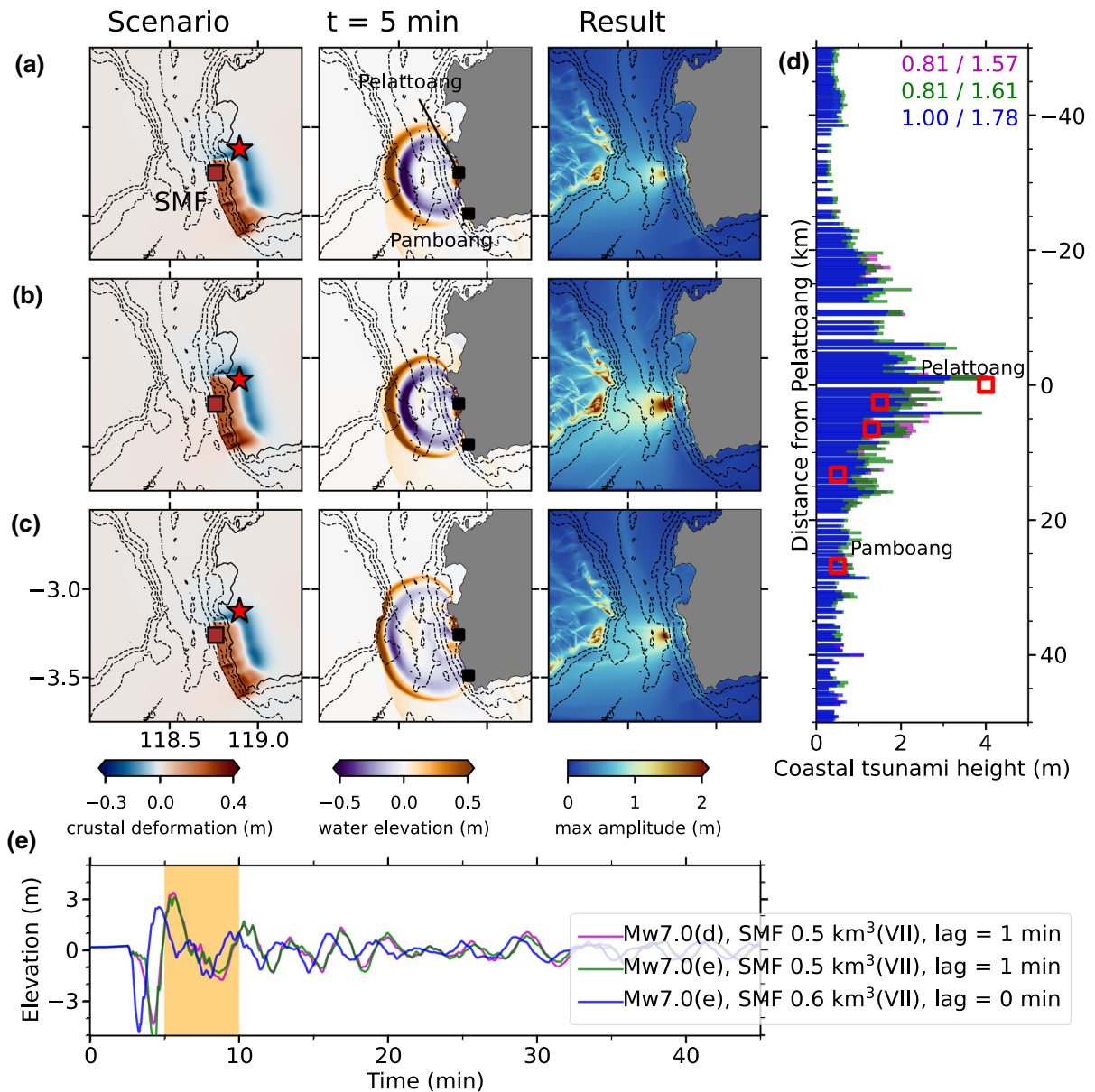


Figure 10

Selected combination of earthquake and submarine mass failure (SMF) tsunami scenarios from **a** rupture model (**d**)—SMF 0.5 km<sup>3</sup>(VII)—lag time 1 min, **b** rupture model (**e**)—SMF 0.5 km<sup>3</sup>(VII)—lag time 1 min, and **c** rupture model (**e**)—SMF 0.6 km<sup>3</sup>(VII)—lag time 0 min. Left to right panels show SMF location and the crustal deformation, tsunami elevation at  $t = 5$  min, and maximum tsunami amplitude. **d** Maximum coastal tsunami heights with numbers show  $K/\kappa$  coefficients. **e** Tsunami waveform at Pelattoang

have been identified at several places, such as at the Haya slide in the west of Mamuju (Nugraha et al., 2020) and eastern offshore of Kalimantan Island with a volume of up to 600 km<sup>3</sup> (Brackenridge et al., 2020).

Our simulations of SMF tsunamis in the Makassar Sea revealed that when a large SMF is located at a shallower depth ( $< 500$  m), it generates an extremely high tsunami (see SMF 0.6 km<sup>3</sup>(IX) and (X) on Figs. 9c and S4a, respectively). Contrary, if it is

located at a deeper depth ( $> 1,500$  m), the resulting tsunami heights are relatively small (SMF  $0.6 \text{ km}^3$ (VI) in Fig. 9a). From 30 simulations (Fig. S4), SMF with volume  $0.6 \text{ km}^3$  that started at depths of 1000 m and 1500 m with failure movement toward the west are the best models to reproduce a high tsunami at Pelattoang (SMF  $0.6 \text{ km}^3$ (VII) and (VIII) on Fig. S4). Tsunami arrival time from these two scenarios are about 5 min (Fig. S4b). By assuming that one of these scenarios is the best to explain the tsunami data (SMF  $0.6 \text{ km}^3$ (VIII) in Fig. 9b), this suggests that there should be a time lag between the earthquake origin time and the starting time of the SMF (Fig. 9e).

When we combined the earthquake and SMF sources for tsunami modelling, the earthquake rupture model and its rupture location contributed insignificantly to the simulated maximum tsunami height (see rupture model (d) and (e) with SMF  $0.5 \text{ km}^3$  and  $t=1$  min in Fig. 10). As expected, increasing the SMF volume and starting the SMF at a shallower water depth resulted in higher coastal tsunami height. We also noticed that delaying the starting time of the SMF increased the final tsunami height. We suspect that superposition between tsunami propagation once generated by the earthquake and the initial wave triggered by the SMF would explain this finding. The combined scenario involving earthquake rupture (e) and SMF  $0.6 \text{ km}^3$ (VII) without any lag time gives  $K = 1.00$  (Fig. 10). However, the maximum simulated tsunami produced is  $\sim 2.5$  m, which is about half the tsunami height observed at Pelattoang. Moreover, in a real event, there is usually a lag time between earthquake origin time and SMF generation (e.g. seconds to minutes). However, it is rather difficult to determine the time as involving a complex combination of the local conditions, such as distance between the earthquake rupture area and unstable land, soil condition, and other factors. In this study, we preferred a lag time of 1 min from the rupture earthquake (e), SMF  $0.5 \text{ km}^3$ (VII), and with a lag time of 1 min that gives  $K = 0.81$  and  $\kappa = 1.57$  (Fig. 10). The tsunami arrival time is about 5 min, which appears to be a reasonable ETA for the eyewitness to run back and warn the villagers (Figs. 10, S5b).

Because a tsunami generated by an earthquake-triggered landslide involves a high-degree uncertainty, in addition to the limited high-resolution DEM and insufficient historical accounts of tsunami data, it is rather difficult to determine a perfect source combination from earthquake and SMF scenarios. We also are unable to exclude another possibility that the earthquake rupture and its deformation are fully inland. There is also a possibility that an unidentified local tectonic fault was responsible for the event. In this case, there would be no complex interaction between the earthquake and the SMF-generated tsunami. As this is the first attempt to reconstruct the source mechanism of the 1969 western Sulawesi earthquake and tsunami event, further study is needed, particularly to confirm the evidence of the SMF at the west offshore of Pelattoang and to provide a more realistic source model.

## 6. Conclusion

In this study, we have shown that historical accounts of the 1969 western Sulawesi, Indonesia, earthquake and tsunami, combined with seismic data, can be used to determine the plausible source mechanism. Through earthquake location and first-motion polarity analyses, we confirmed that the event was triggered by an Mw 7.0 inland and shallow crustal fault earthquake, possibly from the eastward-dipping Makassar Thrust fault. The ground motion modelling based on a trial-and-error approach by shifting the rupture model area was able to reconstruct the earthquake intensity data. It shows that the rupture model Mw7.0 (f) is the best fit to explain the observation. However, the earthquake rupture model alone is unable to reproduce the unusually high 4-m tsunami at Pelattoang. The  $I_2$  analysis indicates that the tsunami height dataset is caused by a landslide source. This observation was able to be reconstructed by a submarine mass failure (SMF) of  $0.6 \text{ km}^3$ . Potentially, a complex interaction between the earthquake and SMF sources were involved in the tsunami generation, in this case rupture model Mw7.0 (f) and SMF  $0.5 \text{ km}^3$ .

### Acknowledgements

We thank Dr. Mohammad Heidarzadeh from Brunel University London, UK, for valuable discussion that significantly improved the initial manuscript. Tsunami simulations were performed on the Young HPC <https://www.rc.ucl.ac.uk/docs/Clusters/Young/> under Brunel University London allocation grant.

**Author Contributions** All authors = prepared manuscript; IRP = lead author, historical accounts, tsunami modelling; AC = tectonic setting, historical accounts, ground motion modelling; HA = earthquake analysis; TB and KI = developed JAGURS code for earthquake and landslide modelling. All authors read and approved the final manuscript.

### Funding

IRP was supported by the Royal Society, United Kingdom (CHLR1180173) during his fellowship at Brunel University London (January 2020 - July 2021).

### Data Availability Statement

V<sub>s30</sub> dataset is available on [https://www.researchgate.net/publication/303989870\\_vs30\\_Indonesia](https://www.researchgate.net/publication/303989870_vs30_Indonesia). Earthquake data catalogue including arrival times and first-motion polarities are available from <https://www.isc.ac.uk/isc-ehb/> (last accessed April 2021). The national bathymetry (BATNAS) and coastal contours bathymetry (Lembar Pantai Indonesia) are freely provided by the Government of Indonesia on <https://tanahair.indonesia.go.id/portal-web> and <https://portal.ina-sdi.or.id/downloadaoi>, respectively (last accessed 22 March 2021).

### Code Availability

Figures were prepared using Quantum GIS, Generic Mapping Tools, and Matplotlib. We used the Scientific Colourmaps (Cramerri et al., 2021) which available on <https://www.fabiocramerri.ch/colourmaps/> (last accessed 22 March 2021). The JAGURS code for tsunamigenic earthquake

modelling is available on <https://github.com/jagurs-admin/jagurs>. The Open Quake software is available on <https://github.com/gem/oq-engine>.

### Declarations

**Conflict of Interest** The authors declare that they have no conflict of interest.

**Publisher's Note** Springer Nature remains neutral with regard to jurisdictional claims in published maps and institutional affiliations.

### REFERENCES

- Aida, I. (1978). Reliability of a tsunami source model derived from fault parameters. *Journal of Physics of the Earth*, 26(1), 57–73. <https://doi.org/10.4294/jpe1952.26.57>.
- Baba, T., Gon, Y., Imai, K., Yamashita, K., Matsuno, T., Hayashi, M., & Ichihara, H. (2019). Modeling of a dispersive tsunami caused by a submarine landslide based on detailed bathymetry of the continental slope in the Nankai trough, southwest Japan. *Tectonophysics*, 768, 228182. <https://doi.org/10.1016/j.tecto.2019.228182>.
- Baba, T., Takahashi, N., Kaneda, Y., Ando, K., Matsuoka, D., & Kato, T. (2015). Parallel implementation of dispersive tsunami wave modeling with a nesting algorithm for the 2011 Tohoku tsunami. *Pure and Applied Geophysics*, 172(12), 3455–3472. <https://doi.org/10.1007/s00024-015-1049-2>.
- Bellier, O., Sébrier, M., Seward, D., Beaudouin, T., Villeneuve, M., & Putranto, E. (2006). Fission track and fault kinematics analyses for new insight into the Late Cenozoic tectonic regime changes in West-Central Sulawesi (Indonesia). *Tectonophysics*, 413(3–4), 201–220. <https://doi.org/10.1016/j.tecto.2005.10.036>.
- Bergman, S. C., Coffield, D. Q., Talbot, J. P., & Garrard, R. A. (1996). Tertiary tectonic and magmatic evolution of western Sulawesi and the Makassar Strait, Indonesia: Evidence for a Miocene continent-continent collision. *Geological Society Special Publication*, 106(1), 391–429. <https://doi.org/10.1144/GSL.SP.1996.106.01.25>.
- Bird, P. (2003). An updated digital model of plate boundaries. *Geochemistry, Geophysics, Geosystems*, 4(3). <https://doi.org/10.1029/2001GC000252>.
- Boore, D. M., Stewart, J. P., Seyhan, E., & Atkinson, G. M. (2014). NGA-west2 equations for predicting PGA, PGV, and 5% damped PSA for shallow crustal earthquakes. *Earthq Spectra*, 30(3), 1057–1085. <https://doi.org/10.1193/070113EQS184M>.
- Brackenkridge, R. E., Nicholson, U., Sapiie, B., Stow, D., & Tappin, D. R. (2020). Indonesian Throughflow as a preconditioning mechanism for submarine landslides in the Makassar Strait. *Geological Society, London, Special Publications*, 500. <https://doi.org/10.1144/SP500-2019-171>
- Cipta, A., Rudyanto, A., Afif, H., Robiana, R., Solikhin, A., Omang, A., & Supartoyo, Hidayati S. (2020). Unearthing the buried Palu–Koro Fault and the pattern of damage caused by the

- 2018 Sulawesi earthquake using HVSR inversion. *Geol Soc Spec Publ* pp SP501–2019–70. <https://doi.org/10.1144/SP501-2019-70>
- Cipta, A., Robiana, R., Griffin, J., Horspool, N., Hidayati, S., & Cummins, P. R. (2017). A probabilistic seismic hazard assessment for Sulawesi, Indonesia. *Geological Society Special Publication*, 441(1), 133–152. <https://doi.org/10.1144/SP441.6>.
- Dowrick, D. J., Hancox, G. T., Perrin, N. D., & Dellow, G. D. (2008). The modified mercalli intensity scale. *Bulletin of the New Zealand National Society for Earthquake Engineering*, 41(3), 193–205. <https://doi.org/10.5459/bnzsee.41.3.193-205>.
- Engdahl, E. R., Giacomo, D. D., Sakarya, B., Gkarlaoui, C. G., Harris, J., & Storchak, D. A. (2020). ISC-EHB 1964–2016, an improved data set for studies of earth structure and global seismicity. *Earth and Space Science*, 7(1). <https://doi.org/10.1029/2019EA000897>.
- Fikrie, M., & Hardiansya, A. (2018). Lembong tallu dan gempa bertubi-tubi di Mamasa. <https://lokadata.id/artikel/lembong-tallu-dan-gempa-bertubi-tubi-di-mamasa>, available on <https://lokadata.id/artikel/lembong-tallu-dan-gempa-bertubi-tubi-di-mamasa>, last accessed 26 February 2021.
- Fitch, T. J. (1972). Plate convergence, transcurrent faults, and internal deformation adjacent to Southeast Asia and the western Pacific. *Journal of Geophysical Research (1896–1977)*, 77(23), 4432–4460. <https://doi.org/10.1029/JB077i023p04432>.
- Fritz, H. M., Kongko, W., Moore, A., McAdoo, B., Goff, J., Harbitz, C., et al. (2007). Extreme runup from the 17 July 2006 Java tsunami. *Geophysical Research Letters*, 34(12). <https://doi.org/10.1029/2007GL029404>.
- Gerardi, F., Barbano, M. S., Martini, P. M. D., & Pantosti, D. (2008). Discrimination of tsunami sources (earthquake versus landslide) on the basis of historical data in eastern Sicily and southern Calabria. *Bulletin of the Seismological Society of America*, 98(6), 2795–2805. <https://doi.org/10.1785/0120070192>.
- Hall, R. (2011). Australia–SE Asia collision: Plate tectonics and crustal flow. *Geological Society, London, Special Publications*, 355(1), 75–109. <https://doi.org/10.1144/SP355.5>.
- Hamilton, W. B. (1979). *Tectonics of the Indonesian region* (Vol. 1078). US Government Printing Office.
- Hardebeck, J. L. (2002). A new method for determining first-motion focal mechanisms. *Bulletin of the Seismological Society of America*, 92(6), 2264–2276. <https://doi.org/10.1785/0120010200>.
- Havskov, J., & Ottemoller, L. (1999). SeisAn earthquake analysis software. *Seismological Research Letters*, 70(5), 532–534. <https://doi.org/10.1785/gssrl.70.5.532>.
- Havskov, J., Voss, P. H., & Ottemöller, L. (2020). Seismological observatory software: 30 year of SEISAN. *Seismological Research Letters*, 91(3), 1846–1852. <https://doi.org/10.1785/0220190313>.
- Hurukawa, N., & Maung, P. M. (2011). Two seismic gaps on the Sagaing Fault, Myanmar, derived from relocation of historical earthquakes since 1918d. *Geophysical Research Letters*, 38(1), n/a. <https://doi.org/10.1029/2010GL046099>.
- Imamura, F., & Imteaz, M. (1995). Long waves in two-layers: Governing equations and numerical model. *Sci of Tsunami Hazards*, 13, 3–24.
- International Tsunami Information Center. (1969a). Makassar Strait earthquake and tsunami - February 23, 1969. In: International Tsunami Information Center Newsletter, vol II, IOC-UNESCO, Hawaii, USA, available on [http://itic.ioc-unesco.org/images/stories/products\\_and\\_services/newsletter/1960-1969/1969/1969\\_Apr.pdf](http://itic.ioc-unesco.org/images/stories/products_and_services/newsletter/1960-1969/1969/1969_Apr.pdf), last Accessed 26 February 2021.
- International Tsunami Information Center. (1969b). Makassar Strait earthquake and tsunami of February 23, 1969 - indonesia. In: International Tsunami Information Center Newsletter, vol II, IOC-UNESCO, Hawaii, USA, available on [http://itic.ioc-unesco.org/images/stories/products\\_and\\_services/newsletter/1960-1969/1969/1969\\_July.pdf](http://itic.ioc-unesco.org/images/stories/products_and_services/newsletter/1960-1969/1969/1969_July.pdf), last Accessed 26 February 2021.
- Jarvis, A., Reuter, H., Nelson, A., & Guevara, E. (2008). Hole-filled SRTM for the globe Version 4. Available from the CGIAR-CSI SRTM 90m Database <http://srtm.csi.cgiar.org>.
- Kajiura, K. (1963). The leading wave of a tsunami. *Bulletin of the Earthquake Research Institute*, 41(4), 535–571.
- Kennet, B. L. N. (1991). IASPEI 1991 seismological tables. *Terra Nova*, 3(2), 122–122. <https://doi.org/10.1111/j.1365-3121.1991.tb00863.x>.
- Latief, H., Puspito, N. T., & Imamura, F. (2000). Tsunami catalog and zones in Indonesia. *Journal of Natural Disaster Science*, 22(1), 25–43.
- Lentas, K. (2017). Towards routine determination of focal mechanisms obtained from first motion p-wave arrivals. *Geophysical Journal International*, 212(3), 1665–1686. <https://doi.org/10.1093/gji/ggx503>.
- Matsuoka, M., Wakamatsu, K., Fujimoto, K., & Midorikawa, S. (2006). Average shear-wave velocity mapping using Japan engineering geomorphologic classification map. *Earthquake Engineering and Structural Dynamics*, 23(1), 57s–68s. <https://doi.org/10.2208/jscseee.23.57s>.
- Nugraha, H. D., Jackson, C. A. L., Johnson, H. D., & Hodgson, D. M. (2020). Lateral variability in strain along a mass-transport deposit (MTD) toewall: A case study from the Makassar Strait, offshore Indonesia. *Journal of the Geological Society*, pp jgs2020–071. <https://doi.org/10.1144/jgs2020-071>.
- Okada, Y. (1985). Surface deformation due to shear and tensile faults in a half-space. *Bulletin of the Seismological Society of America*, 75(4), 1135–1154.
- Okal, E. A., & Synolakis, C. E. (2004). Source discriminants for near-field tsunamis. *Geophysical Journal International*, 158(3), 899–912. <https://doi.org/10.1111/j.1365-246x.2004.02347.x>.
- Pagani, M., Monelli, D., Weatherill, G., Danciu, L., Crowley, H., Silva, V., et al. (2014). OpenQuake engine: An open hazard (and risk) software for the Global Earthquake Model. *Seismological Research Letters*, 85(3), 692–702. <https://doi.org/10.1785/0220130087>.
- Peterson, J. R., & Hutt, C. R. (2014). *World-wide standardized seismograph network: A data users guide*. <https://doi.org/10.3133/ofr20141218>
- Prasetya, G., De Lange, W., & Healy, T. (2001). The Makassar Strait tsunamigenic region, Indonesia. *Natural Hazards*, 24(3), 295–307. <https://doi.org/10.1023/a:1012297413280>.
- Pusat Studi Gempa Nasional. (2018). Peta sumber dan bahaya gempa indonesia tahun 2017. Tech. rep., Ministry of Public Works of Indonesia. Available on <https://simantu.pu.go.id/content/?id=3605> in Bahasa Indonesia (last Accessed 26 February 2021).
- Rangin, C., Pichon, X. L., Mazzotti, S., Pubellier, M., Chamot-Rooke, N., Aurelio, M., et al. (1999). Plate convergence measured by GPS across the Sundaland/Philippine Sea Plate deformed boundary: The Philippines and eastern Indonesia. *Geophysical Journal International*, 139(2), 296–316. <https://doi.org/10.1046/j.1365-246x.1999.00969.x>.

- Reasenber, P., & Oppenheimer, D. (1985). Fpfit, fplot and fpage: Fortran computer programs for calculating and displaying earthquake fault-plane solutions. *Technology Reports*. <https://doi.org/10.3133/ofr85739>.
- Rudyanto, A. (2014). Development of strong-motion database for the Sumatra-Java region. PhD thesis, Research School of Earth Sciences, the Australian National University, Canberra, Australia. <https://doi.org/10.25911/5c6e706d3ca39>. <http://hdl.handle.net/1885/155705>
- Satake, K., Hirata, K., Yamaki, S., & Tanioka, Y. (2006). Re-estimation of tsunami source of the 1952 Tokachi-oki earthquake. *Earth Planets Space*, 58(5), 535–542. <https://doi.org/10.1186/BF03351951>.
- Satyana, A. H., Faulin, T., & Mulyati, S. N. (2011). Tectonic evolution of Sulawesi area: Implications for proven and prospective petroleum plays. In *Proceeding of The 36th HAGI and 40th IAGI 2011 Annual Convention and Exhibition, Makassar*.
- Silver, E. A., McCaffrey, R., Joyodiwiryo, Y., & Stevens, S. (1983). Ophiolite emplacement by collision between the Sula Platform and the Sulawesi Island Arc, Indonesia. *The Journal of Geophysical Research: Solid Earth*, 88(B11), 9419–9435. <https://doi.org/10.1029/JB088iB11p09419>.
- Snoke, J. A. (2003). Focmec: FOCal MECHANISM Determinations. In W. H. Lee, H. Kanamori, P. C. Jennings, & C. Kisslinger (Eds.), *International handbook of earthquake and engineering seismology, part b, international geophysics* (Vol. 81, pp. 1629–1630). Academic Press. [https://doi.org/10.1016/S0074-6142\(03\)80291-7](https://doi.org/10.1016/S0074-6142(03)80291-7).
- Soetardjo, Untung M., Arnold, E., Soetadi, R., Ismail, S., & Kertapati, E. K. (1985). Series on Seismology Volume V: Indonesia. U.S. Geological survey.
- Soloviev, S., Go, C., & Kim, K. (1992). Catalog of tsunamis in the Pacific. Academy of Sciences of the USSR, Moscow, translated from Russian by Amerind Publishing Co. Pvt. Ltd., New Delhi (1988).
- Synolakis, C. E. (1991). Tsunami runup on steep slopes: How good linear theory really is. In *Tsunami Hazard* (pp. 221–234). Springer. [https://doi.org/10.1007/978-94-011-3362-3\\_8](https://doi.org/10.1007/978-94-011-3362-3_8)
- ten Brink, U., Lee, H., Geist, E., & Twichell, D. (2009). Assessment of tsunami hazard to the U.S. East Coast using relationships between submarine landslides and earthquakes. *Marine Geology*, 264, 65–73. <https://doi.org/10.1016/j.margeo.2008.05.011>.
- Thingbaijam, K. K. S., Mai, P. M., & Goda, K. (2017). New empirical earthquake source-scaling laws. *Bulletin of the Seismological Society of America*, 107(5), 2225–2246. <https://doi.org/10.1785/0120170017>.
- Tinti, S., Armigliato, A., Manucci, A., Pagnoni, G., Zaniboni, F., Yalçiner, A. C., & Altinok, Y. (2006). The generating mechanisms of the August 17, 1999 izmit bay (turkey) tsunami: Regional (tectonic) and local (mass instabilities) causes. *Marine Geology*, 225(1–4), 311–330. <https://doi.org/10.1016/j.margeo.2005.09.010>.
- Tsuji, Y., Matsutomi, H., Imamura, F., Takeo, M., Kawata, Y., Matsuyama, M., et al. (1995). Damage to coastal villages due to the 1992 flores island earthquake tsunami. *Pure and Applied Geophysics PAGEOPH*, 144(3–4), 481–524. <https://doi.org/10.1007/BF00874380>.
- van Leeuwen, T., & Pieters, P. E. (2012). Mineral deposits of Sulawesi. In: Proceedings of The Sulawesi Mineral Resources 2011, Seminar MGEI-IAGI, 28–29 November 2011, Manado, Indonesia.
- Virtanen, P., Gommers, R., Oliphant, T. E., Haberland, M., Reddy, T., Cournapeau, D., et al. (2020). SciPy 1.0: Fundamental algorithms for scientific computing in Python. *Nature Methods*, 17(3), 261–272. <https://doi.org/10.1038/s41592-019-0686-2>.
- Wald, D. J., Quitoriano, V., Heaton, T. H., & Kanamori, H. (1999). Relationships between Peak Ground Acceleration, Peak Ground Velocity, and Modified Mercalli Intensity in California. *Earthquake Spectra*, 15(3), 557–564. <https://doi.org/10.1193/1.1586058>.
- Weston, J., Engdahl, E. R., Harris, J., Giacomo, D. D., & Storchak, D. A. (2018). ISC-EHB: Reconstruction of a robust earthquake data set. *Geophysical Journal International*, 214(1), 474–484. <https://doi.org/10.1093/gji/ggy155>.

(Received August 25, 2021, revised May 10, 2022, accepted May 11, 2022, Published online June 11, 2022)